



Activation of MoS₂ via tungsten doping for efficient photocatalytic oxidation of gaseous mercury

Jun Cai^a, Yi Xia^{a,b,*}, Ruiqi Gang^b, Sufang He^a, Sridhar Komarneni^{c,**}

^a Research Center for Analysis and Measurement, Kunming University of Science and Technology, and Analytic & Testing Research Center of Yunnan, Kunming 650093, China

^b The Key Laboratory of Unconventional Metallurgy, Ministry of Education, Faculty of Metallurgical and Energy Engineering, Kunming University of Science and Technology, Kunming 650093, China

^c Department of Ecosystem Science and Management and Materials Research Institute, 204 Energy and the Environment Laboratory, The Pennsylvania State University, University Park, PA 16802, USA

ARTICLE INFO

Keywords:

Molybdenum disulfide
Tungsten doping
Photocatalysis
Sulfur defects
Gaseous mercury

ABSTRACT

Defect engineering and heterogeneous doping are considered as the effective routes to improve the photocatalytic activity of MoS₂. In this study, tungsten was used to produce sulfur defects and tungsten doping on MoS₂ by one step hydrothermal treatment. Tungsten doping not only promotes the formation of sulfur defects, but also accelerates the efficiency of separation and transfer of electron-hole pairs, which enables the samples to maintain high catalytic oxidation activity for a long time. Furthermore, comparative experiments show that sulfur defects can promote the activation of O₂ and the formation of more active O₂ and ·OH species. As a result, the W-doped MoS₂ exhibited a high removal efficiency of more than 99% of gaseous mercury. In addition, W-doped MoS₂ showed good stability, long term durability, enhanced water and sulfur resistance under light illumination. This work provides a novel direction for designing efficient photocatalysts based on transition metal dichalcogenides.

1. Introduction

Atmospheric heavy metal pollution is an important source of heavy metal pollution [1]. Because of their highly mobility, wide coverage, non-degradability, bio-toxicity, and bio-accumulation [2], atmospheric heavy metals cause serious consequences for human health and environmental safety. Most smelting flue gases are difficult to manage due to their large exhaust emissions, high dust content, and complex heavy metal composition, and traditional technologies fail to achieve the desired management effect. Accordingly, one of the most pressing challenges in this field is to develop new technologies for the heavy metal pollution treatment [3–5].

Due to their abundant active sites and highly noble metal-like characteristics, transition metal dichalcogenides (TMDs) are considered as one of the best type of photocatalytic materials in the development of non-noble metal nano-catalysts [6,7]. According to recent studies, TMDs with excellent catalytic activity and durability have demonstrated superior success in water pollution treatment [8,9].

Despite numerous studies of pollution treatment, it is still a major challenge to improve the active sites, catalytic performance, catalytic stability and contaminant resistance in order to meet the strict requirements of practical applications [10,11].

Recently, sulfur vacancies in the basal plane of TMDs have been proven to be catalytic sites, and the gap states near the Fermi level enable hydrogen to directly bind with exposed molybdenum atoms [12]. So far, there are only limited approaches to remove sulfur from the basal planes of 2D TMD materials, such as electrochemical reduction, H₂ annealing, and argon plasma exposure [13–15]. However, these methods are very complicated to implement and prone to cause danger due to the high temperature. Therefore, it is urgent to develop an effective, safe and economical strategy to remove chalcogen atoms from the basal planes of TMDs. Molybdenum sulfide (MoS₂), the star member of the TMDs family, has been extensively studied as a potential catalyst in various areas due to its excellent electrical conductivity and good stability [16–18]. Ge et al. obtained an efficient HER catalyst using single-atom Ru and Ni co-modified MoS₂ [19]. Hu et al. achieved a

* Corresponding author at: Research Center for Analysis and Measurement, Kunming University of Science and Technology, and Analytic & Testing Research Center of Yunnan, Kunming 650093, China.

** Corresponding author.

E-mail addresses: xiayi0125@163.com (Y. Xia), sxk7@psu.edu (S. Komarneni).

<https://doi.org/10.1016/j.apcatb.2022.121486>

Received 21 February 2022; Received in revised form 19 April 2022; Accepted 6 May 2022

Available online 11 May 2022

0926-3373/© 2022 Elsevier B.V. All rights reserved.

H₂/CO ratio of 0.35–3.6 in syngas by selectively decorating MoS₂ with size-controlled (1–50 nm) gold nanoparticles [20]. Sun et al. found that the presence of highly accumulated electrons in gold-loaded ultrathin MoS₂ under illumination could lead to superior performance in the reduction of CO₂ to methane [21].

In this study, sulfur defects-enriched MoS₂ was prepared via tungsten doping by a low-temperature hydrothermal treatment. The morphology, phase composition, chemical composition, and elemental valence of the prepared catalysts were characterized. The Hg⁰ removal efficiency, durability and stability of W-MoS₂ were studied, and the effect of flue gas composition was also considered. Finally, a possible mechanism for the catalytic removal of Hg⁰ catalyzed by W-MoS₂ was proposed.

2. Experimental section

2.1. Materials

Both (NH₄)₆Mo₇O₂₄·4H₂O and H₂NCSHN₂ were provided by Jindong Tianzheng Fine chemical Reagent Factory (Tianjin, China), and WCl₆ was obtained from Aladdin Biochemical Technology Co., Ltd (Shanghai, China). In this study, all chemical reagents were used without further treatment, and ultrapure water was used to prepare all solutions.

2.2. Preparation of W-MoS₂ samples

In this study, 0.35 g of ammonium molybdate was dissolved in ultrapure water (15–20 mL) under stirring, and then 0.1 g of tungsten chloride was added and completely dispersed, and finally 0.1 g of thiourea was added and stirred until the color of the solution remained unchanged [10,22]. Thereafter, the solution was added into a stainless-steel autoclave lined with PTEE with the volume of 100 mL and maintained in an oven at 180 °C for different times to determine the role of time on crystallization. After the reaction, the autoclave was cooled to room temperature in air naturally, and the obtained product was filtered and washed several times with ethanol and ultrapure water, and then dried at 80 °C for 10 h. The W-MoS₂ samples prepared at different reaction times of 6 h, 9 h, and 12 h were denoted as W-MoS₂-6 h, W-MoS₂-9 h and W-MoS₂-12 h, respectively. Pure products of MoS₂ and WS₂ were also prepared under the determined optimum reaction time for W-MoS₂. The specific synthesis process is displayed in Fig. 1.

2.3. Characterization

X-ray diffraction (XRD) patterns were obtained from a LynxEye array diffractometer (D8 FOCUS, Bruker, Germany) with CuKα radiation at 40 kV and 40 mA in the 2θ range of 5–90° with the step size of 0.02° and the measurement step and time delay were 0.011 s and 100 s,

respectively. Scanning electron microscopy (SEM, Quanta 200, FEI, US) and High-resolution transmission electron microscopy (HRTEM, Type, FEI, US) were employed to obtain the micromorphological images of the samples. X-ray energy spectroscopy (XPS, Escalab 250, Thermo Scientific, US) using a K-α ray source unit was used to analyze the sample surface, and the binding energy was corrected for the standard of surface carbon C1s (284.8 eV). The N₂ adsorption-desorption isotherms were obtained using an adsorption unit (ASAP 2020, Micromeritics, US) at liquid nitrogen temperature. The Brunauer-Emmett-Teller (BET) equation was used to determine the specific surface area and pore volume of samples. The photoluminescence (PL) spectra of samples were obtained by a spectrophotometer (F-7000, Hitachi, Japan) at room temperature with the excitation wavelength of 325 nm. Radical species were analyzed by electron spin resonance (ESR, A300, Bruker, Germany). ICP (Teledyne Leeman Labs Prodigy, USA) was used to determine the contents of S and Mo elements.

2.4. Photocatalytic activity test

The experimental setup is displayed in Fig. S1. It is composed of flue gas simulation system, Hg⁰ generator, photocatalytic reactor, mercury detector and tail gas absorption system. The simulated flue gas had a total flow rate of 400 mL/min. To guarantee a constant mercury permeation rate, the mercury permeation tube of Hg⁰ generator was located in a U-shaped glass tube, which was immersed in a water bath at constant temperature. The inlet Hg⁰ concentration was controlled at 400 µg/m³, and the gas contained 4 vol% trace oxygen.

The photocatalytic reactor is composed of an opaque shell, a straight quartz tube and a 9 W ultraviolet lamp (TUV PL-S, Philips, the Netherlands). The wavelength of ultraviolet light used was 360 nm, the intensity of ultraviolet lamp was 3 MW/cm², and the ultraviolet energy density was 540 J/L. The experimental procedures are as follows: 50 mg catalyst was placed on the quartz sand in a straight quartz tube, followed by introducing the simulated flue gas. The photocatalytic experiment was divided into two parts: dark adsorption and light irradiation. First, the catalyst was subjected to the flue gas to reach an adsorption-desorption equilibrium in the dark for 10 min. Then the ultraviolet lamp was turned on to start the photocatalytic reaction at room temperature. The on-line mercury detector (VM-3000, Mercury Instruments, Germany) was applied to measure the Hg⁰ concentration at the outlet of the reactor. Potassium permanganate solution was arranged at the tail gas outlet to absorb the downstream waste gas [23].

Catalytic efficiency of Hg⁰ (η_{oxi}) was calculated by Eq. (1).

$$\eta_{\text{oxi}}(\%) = \frac{[\text{Hg}^0]_{\text{in}} - [\text{Hg}^0]_{\text{out}}}{[\text{Hg}^0]_{\text{in}}} \times 100\% \quad (1)$$

where, η_{oxi} was the oxidation efficiency of Hg⁰, and $[\text{Hg}^0]_{\text{in}}$ and $[\text{Hg}^0]_{\text{out}}$ were the corresponding Hg⁰ concentrations of the inlet and outlet gas phases, respectively.

3. Results and discussions

3.1. Characterization of W-MoS₂ samples

In this study, sulfur-defect-enriched MoS₂ was obtained by tungsten doping under a facile one-step hydrothermal route. Compared with the previously reported doping methods using metals such as Pd or Zn [13, 24], the tungsten doping in this study is easier to achieve, because its valence state and atomic radius (139 pm) are similar to molybdenum. As shown in Fig. 2(a), the W-MoS₂ sample is in the form of nanospheres with an average diameter of about 600 nm. The magnified SEM image (Fig. 2(b)) reveals that the 3D flower-like nanospheres contain multiple self-assembled thin nanosheets, and the average thickness of the nanosheets grown in all directions is 8 nm, indicating high homogeneity and small size of the nanospheres [25,26]. All of these structures can provide

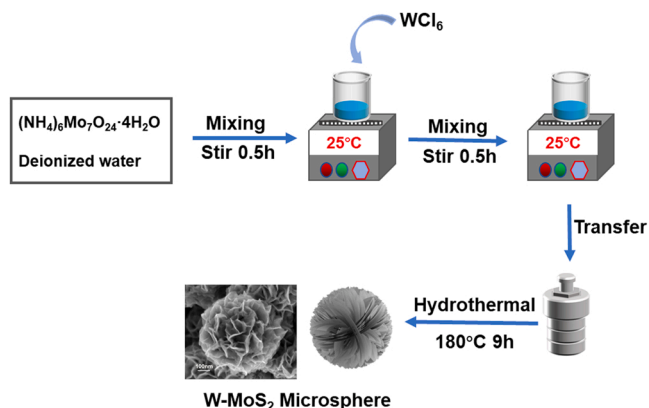


Fig. 1. Schematic diagram of the synthesis of W-MoS₂ microsphere.

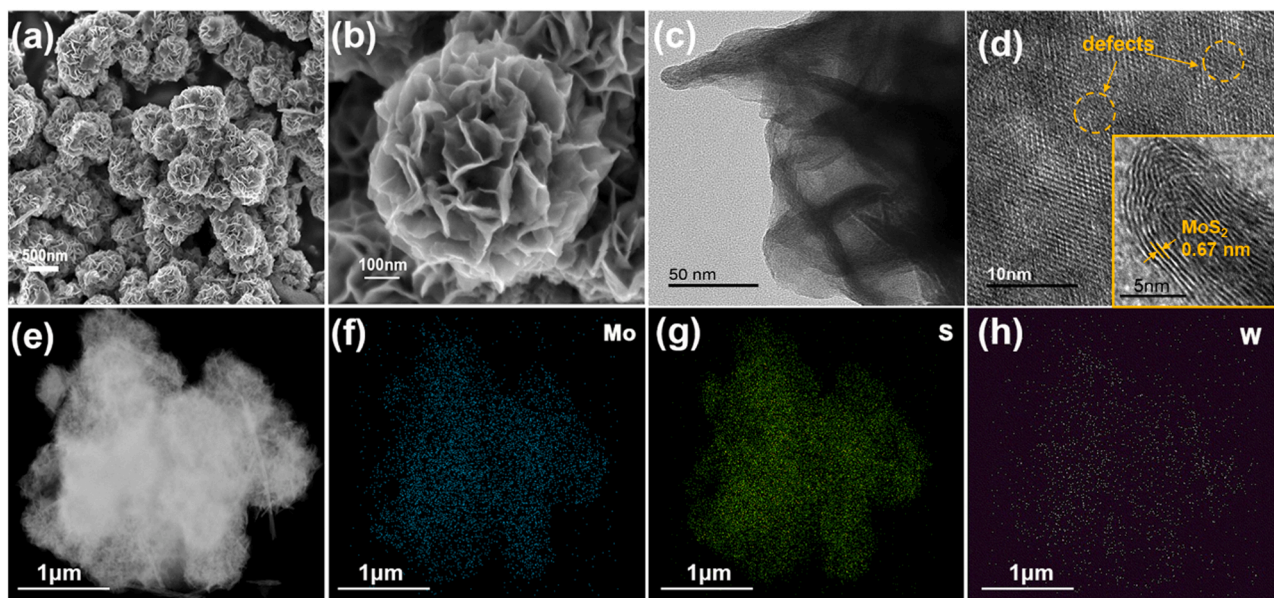


Fig. 2. SEM images of the prepared W-MoS₂ microspheres (a) and magnified image (b); (c) and (d), HRTEM images of W-MoS₂-9 h nanosheets; (e) image of the W-MoS₂-9 h nanosheets for EDS analysis; (f), (g) and (h), the corresponding EDS elemental mapping of W, Mo and S elements.

more active sites, thus improving the catalytic activity. Furthermore, compared with MoS₂ prepared under the same conditions (Fig. S2), the morphology of the sample before and after doping remains unchanged.

HRTEM was used to investigate the binding mode of samples. As shown in Fig. 2(c), the nano-petal of the flower-like nanosphere exhibits random elastic deformation and curved edges, which is more conducive to the stability of the sample [27–32]. As can be seen in Fig. 2(d), discontinuous lattice arrangements and distorted lattice streaks indicate that many defects may have formed in the material. The W-MoS₂ sample has a layered stacking structure, and the plane spacing of the nanosheets is 0.67 nm, which is increased from 0.62 nm of the undoped MoS₂, indicating that lattice distortion occurs during doping. It further indicates that the samples prepared are rich in defects [33]. This unique structure will not only facilitate the charge transfer between Mo and W, but also significantly improves the catalytic performance through the synergistic effect.

EDS elemental mapping was used to investigate the uniformity of samples. The Mo, S, and W elements are uniformly dispersed in the sample, as shown in Fig. 2(e–h), indicating that W has been successfully doped on MoS₂. Tungsten doping may promote the formation of defects. This could broaden the light absorption range of the sample, enhance the separation efficiency of photogenerated carriers, and thus improve the catalytic performance of the sample.

As shown in Fig. 3, the influence of hydrothermal time on doping was

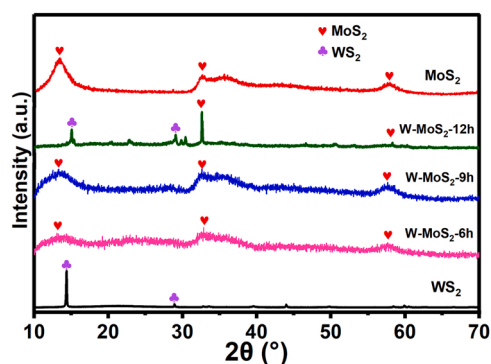


Fig. 3. XRD patterns of MoS₂, WS₂ and W-MoS₂ prepared at different hydrothermal treatment times.

analyzed by XRD. It can be seen that when the hydrothermal time is less than 9 h, the sample is mainly in the pure phase of MoS₂, while when the hydrothermal time is longer than 9 h, the sample is a composite of MoS₂ and WS₂. The W-MoS₂-9 h sample has better crystallinity, and the shift in the characteristic peaks indicates that the doping is relatively successful. The diffraction peaks at 13° and 33.5° belong to the (103) and (110) crystal planes of MoS₂, respectively, and 14° corresponds to the (002) crystal plane of WS₂ [34–36]. Furthermore, the peak of (002) crystal plane of WS₂ in doped samples shifts to a lower angle, indicating an increase in the lattice constant. This is consistent with the findings of HRTEM in Fig. 2 and suggests that tungsten doping will lead to the accumulation of a number of defects in MoS₂. According to the ICP results of S measurements for MoS₂ and W-MoS₂, the Mo:S and (W + Mo) ratios are 1:1.97 and 1:1.82, respectively. It can be concluded that the defects introduced in W-MoS₂-9 h sample are mainly sulfur defects. Thus, sulfur defect-enriched W-MoS₂ sample (W-MoS₂-9 h) was successfully prepared. In addition, the W-MoS₂-12 h sample can be found to have both MoS₂ and WS₂ diffraction peaks. This indicates that at a hydrothermal treatment time of 12 h, the element W is no longer doped into MoS₂, but a composite of MoS₂ and WS₂ was formed. The catalytic performance of the MoS₂ and WS₂ composites is significantly reduced when compared to the W-MoS₂ heterojunction.

XPS was used to study the chemical composition, elemental valence and defect types of the prepared samples. As shown in Fig. S3, the peaks of Mo 3d, W 4f, S 2p, and O 1s can be clearly observed in the XPS spectra of W-MoS₂ [37–40], and the H₂O absorbed on the sample surface may result in the signal of O 1s Fig. 4(a) shows the high-resolution spectra of Mo 3d. It indicates that the Mo 3d peak of W-MoS₂ shifts to the direction of low binding energy, which may be due to the changed energy state of the Mo external electrons in MoS₂ after tungsten doping [41]. In addition, it can also be seen that Mo (III) and Mo (IV) coexist. When paired with an extra redox couple, the redox reaction occurs at the MoS₂/gas interface. The molybdenum redox reaction will produce structural vacancies on the surface of MoS₂, that is, Mo (III) oxidation will produce molybdenum vacancies, and at the same time, sulfur vacancies caused by Mo (IV) reduction will be formed. The core level S 2p peaks of pure MoS₂ at 162.58 eV and 163.73 eV shift to high energy direction by 0.85 and 0.7 eV after tungsten doping, respectively as shown previously [13,42]. This is because the positively charged sulfur vacancies in W-MoS₂ could significantly reduce the total electron

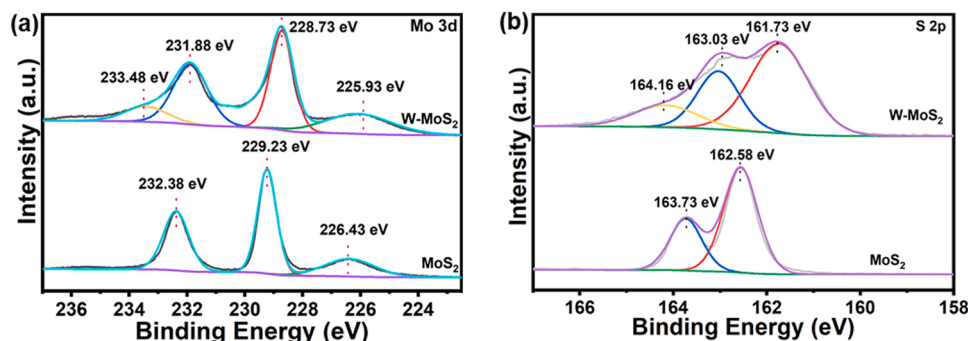


Fig. 4. XPS spectra of MoS₂ and W-MoS₂-9 h sample: (a) Mo 3d and (b) S 2p.

density, thereby increasing the binding energy of the surrounding sulfur species. Apart from the core level peaks, a new set of weak wave peaks in W-MoS₂, also indicate the existence of sulfur vacancies [43]. Meanwhile, the S:Mo ratios in MoS₂ and W-MoS₂ were consistent with the ICP detection results according to the XPS semi-quantitative results. Therefore, it could be inferred that sulfur defect-enriched W-MoS₂ sample (W-MoS₂-9 h) was successfully prepared.

3.2. Photocatalytic properties

3.2.1. Characterization of photocatalytic performance

The performance of Hg⁰ removal by photocatalytic oxidation of the samples prepared with various hydrothermal reaction times was evaluated in this study. As shown in Fig. 5(a), with the increase of photocatalytic time, W-MoS₂-9 h always maintains the highest Hg⁰ removal efficiency. Fig. 5(b) shows that the Hg⁰ removal efficiencies of MoS₂, W-MoS₂-6 h, W-MoS₂-9 h and W-MoS₂-12 h are 90.725%, 94.525%, 99.025%, and 94.275%, respectively, which indicates that doped samples have higher removal efficiencies and showed an improvement in their photocatalytic performance. As shown in Fig. 5(c), when the light is turned off after the photocatalytic reaction, the catalytic efficiency dropped rapidly to zero, which proves that the catalytic effect mainly originated from light exposure. The W-MoS₂-9 h sample has the best performance, and its photocatalytic efficiency is increased by 8.3% compared to the pure MoS₂. Fig. 5(c) also shows that when W-MoS₂-9 h was also exposed to visible light ($\lambda = 420$ nm) irradiation, its Hg⁰ removal efficiency could still reach 76%, suggesting that this photocatalyst has good application potential.

The reusability and durability of W-MoS₂-9 h photocatalyst were also tested. As shown in Fig. 6(a), the Hg⁰ removal efficiency of W-MoS₂-9 h remains basically stable after five cycles, indicating the excellent reusability of this sample. Fig. 6(b) indicates that W-MoS₂-9 h has the

best durability, and it can last for 63 h at the removal efficiency of more than 90%, which is more than 20 times longer than that of the pure MoS₂. This suggests that W-MoS₂-9 h not only has excellent catalytic performance, but also has good durability and stability. Compared with the previous studies in Table 1, W-MoS₂-9 h in this study shows higher catalytic efficiency and capacity when exposed to both ultraviolet and visible light. Besides, W-MoS₂-9 h in this study has higher removal capacity under ultraviolet irradiation than conventional thermal catalysis, indicating that this photocatalytic technology has great application prospects.

The crystalline structure of the samples before and after the reaction was also analyzed by XRD. As shown in Fig. S5, the XRD patterns showed that the crystalline shape of the sample did not change significantly before and after the reaction. These results further confirm the stability of the sample.

3.2.2. Effect of flue gas composition

The real flue gas in zinc smelting mainly consists of nitrogen, sulfur dioxide, oxygen, and other components. In order to broaden the application range of the prepared samples, it is necessary to investigate the influence of real flue gas on their photocatalytic performance, as shown in Fig. S4.

As the primary composition of the flue gas, the influence of O₂ concentration on the Hg⁰ removal efficiency is critical. The Hg⁰ removal efficiencies by photocatalytic oxidation of the photocatalysts under pure N₂ and 4 vol% or 8 vol% O₂ are shown in Fig. S3. At 4 vol% and 8 vol% O₂, the removal efficiencies are 99.03% and 99.23%, respectively, which suggests that increasing the oxygen content is helpful to promote the catalytic reaction. Combined with previous research findings [49], it is determined that the gas-phase O₂ in flue gas could supplement chemisorbed oxygen as well as promote the regeneration of lattice oxygen, both of which are favorable components for the photocatalytic

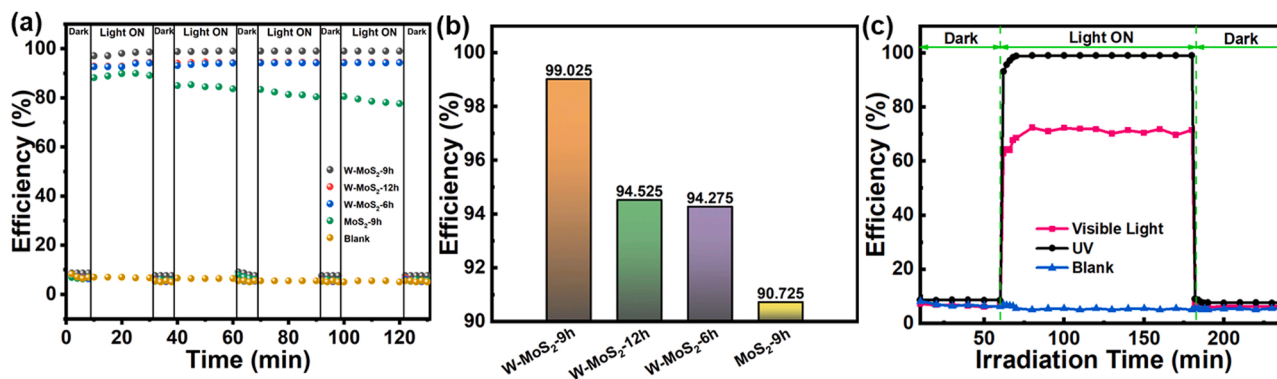


Fig. 5. (a) Comparison of the photocatalytic removal efficiency of Hg⁰ by W-MoS₂, MoS₂ and blank test under ultraviolet irradiation. (b) Highest removal efficiency of all samples under ultraviolet irradiation. (c) Comparison of the photocatalytic removal efficiency of Hg⁰ by W-MoS₂-9 h under ultraviolet and visible light irradiation and blank.

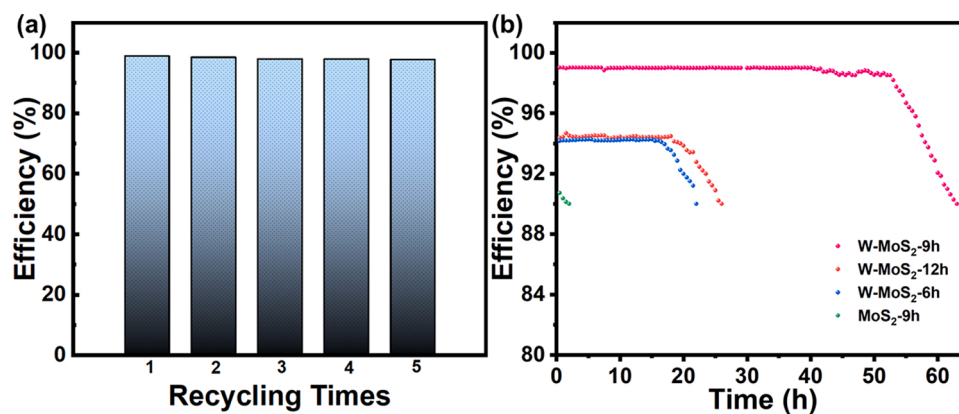


Fig. 6. (a) Cyclability of W-MoS₂-9 h in five cycles. (b) Hg⁰ removal efficiency for different hydrothermal treatment times.

Table 1

Catalytic performance comparison of gaseous mercury in related reports. ^a.

Photocatalysts	Maximum removal Efficiency (%)	Maximum removal capacity (μg Hg ⁰ / mg catalyst)	References
BiOI ₃ /g-C ₃ N ₄ /MoS ₂ (VL)	70.58	/	[44]
BiOX (X=Cl, Br, I) (UV)	96.83	2.03	[45]
Mn-Ce-TiO ₂ (TC)	95.2	0.34	[46]
Fe ₅ Ce ₅ Ti (UV)	91.13	6.89	[23]
CeO ₂ /BiOBr/rGO (VL)	76.53	0.648	[47]
Mo/C500 (TC)	74	0.16	[48]
MF-10 (TC)	100	1.08	[49]
BiOI-390 (VL)	76	/	[50]
W-MoS ₂ -9 h (UV)	99.03	11.98	This work
W-MoS ₂ -9 h (VL)	76	/	This work

^a VL: visible light; UV: ultraviolet light; TC: thermal catalysis.

oxidation reaction. Since increasing the oxygen concentration has limited effect on Hg⁰ removal efficiency, oxygen content of 4 vol% was still selected in this study.

SO₂ is also a major component of zinc smelting flue gas, and sulfur resistance is an important factor for photocatalysts. As shown in Fig. S4, when the SO₂ concentration reaches 200 and 400 ppm, the Hg⁰ removal efficiencies are 85.62% and 78.23%, respectively, indicating that the existence of SO₂ could decrease the removal efficiency. The interaction between the photocatalyst and SO₂ may result in this slight decrease in the removal efficiency. Previous research [47] has found that the adsorption homogeneity of SO₂ and Hg⁰ leads to this decrease. Nonetheless, compared with the published sulfur resistance (the removal efficiency is reduced to 75% at 150 ppm and 57% at 300 ppm) studies, W-MoS₂-9 h in this study has higher sulfur resistance.

As another major influencing factor in flue gas, H₂O acts as an inhibitor for the catalytic reaction, as shown in Fig. S4. When the feed gas contained 5 vol% or 10 vol% H₂O, the Hg⁰ removal efficiency decreased. This is due to the decrease of active sites on the surface caused by the adsorption and coverage of water vapor on the catalyst surface, resulting in a significant decrease in the catalytic capacity of Hg⁰. However, the photocatalytic performance of W-MoS₂-9 h can still maintain at 73.13% and 65.22% in presence of H₂O, indicating that desorption of adsorbed water can be promoted by photoinduced photogenic carrier to enhance the moisture resistance of samples.

3.3. Photocatalysis mechanism

BET and PL analysis were carried out to study the enhanced

photocatalytic performance of W-MoS₂.

Table S1 shows that the specific surface areas of W-MoS₂ prepared at different hydrothermal synthesis times of 6, 9, and 12 h are 29.39, 95.03, and 42.45 m²/g, respectively, which increased first and then decreased with the increase of the hydrothermal time. W-MoS₂-9 h has the largest specific surface area. Furthermore, the pore volume of W-MoS₂-9 h is slightly higher than that of the other two samples. The large specific surface area and pore volume of W-MoS₂-9 h could have a significant impact on their photocatalytic performance, which was confirmed by experiments. As a result, the specific surface area of W-MoS₂-9 h has a favorable response, which is one of the determining factors of the catalytic performance in this study.

The Barrett-Joyner-Halenda (BJH) method was used to obtain nitrogen adsorption-desorption isotherms. The wide hysteresis lines in Fig. 7(a) indicate that the prepared samples have mesoporous structure. The N₂ adsorption-desorption isotherms of the samples have IV type H₃ hysteresis loop line according to the IUPAC classification. The adsorption hysteresis loops appear at relatively high pressures of 0.8–1.0, indicating capillary condensation of the porous adsorbent. Furthermore, W-MoS₂-9 h has higher adsorption, indicating that it might be better encapsulated by disordered pores of larger than 10 nm. All these observations are consistent with the above analysis of W-MoS₂-9 h nanoflowers.

The separation efficiency of electron-hole pairs in prepared samples was studied by PL spectroscopy. As shown in Fig. 7(b), there is a strong emission peak at around 355 nm (subject to excitation at 315 nm), which is attributed to the presence of electron-hole pair recombination. Fig. 7(b) indicates that the electron-hole recombination probability of W-MoS₂-9 h is the lowest. The doped samples have obviously lower peak intensity than that of pure MoS₂, which suggests that the complexation of electron-hole pairs could be effectively suppressed by tungsten doping. It can also be seen that W-MoS₂-12 h showed an emission peak with slightly higher intensity than that of W-MoS₂-6 h, indicating the better electron-hole separation efficiency of W-MoS₂-6 h. As shown in the XRD results, the samples prepared at 6 h were mainly W-doped, while the samples prepared at 12 h were mainly based on WS₂ and MoS₂ composites. This suggests that doping may be more favorable for electron transport than composites, resulting in a lower photogenerated electron-hole recombination rate. This result further proves that doping is a better means of enhancing electron transportation.

To gain more insight into the photocatalytic reaction, XPS and EDS mapping were used to analyze the final products after reaction. The Hg 4f spectrum of the W-MoS₂-9 h sample after reaction is shown in Fig. 8 (a). The peaks at 104.73 and 100.68 eV correspond to Hg 4f_{7/2} and Hg 4f_{5/2} of HgO, respectively. The disappearance of Hg⁰ peaks indicates that it was photocatalytically oxidized and adsorbed on the surface of W-MoS₂-9 h in the form of HgO. The elemental mapping in Fig. 8(b-e) reveals that Mo, S, W, and Hg remain stable in the sample after reaction.

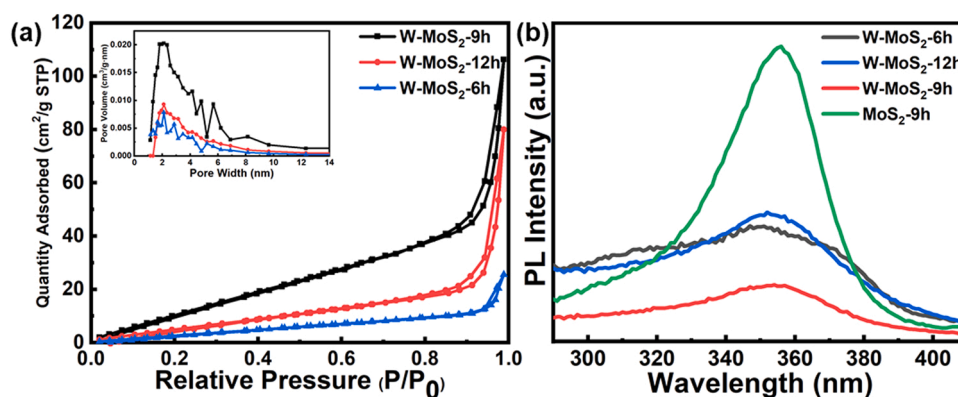


Fig. 7. (a) Nitrogen adsorption-desorption isotherms and pore size distribution curve (inset) of W-MoS₂ samples prepared using different times; (b) PL spectra of W-MoS₂ samples prepared using different times and pure MoS₂ prepared using 9 h.

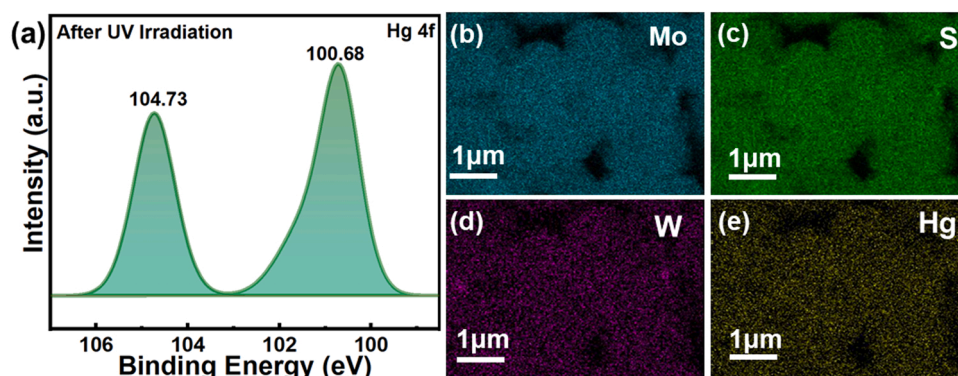


Fig. 8. Hg 4 f XPS spectrum (a) and EDS elemental mapping of the W-MoS₂-9 h sample after reaction.

The above analysis suggests that W-MoS₂-9 h in this study can effectively oxidize Hg⁰ into HgO.

ESR detection was applied to investigate the effect of active oxygen species on the photocatalytic oxidation of Hg⁰. DMSO was used to capture the two free radicals including O₂^{•-} and ·OH [51], and both the signals were detected by ultraviolet light excitation of 365 nm in our system, as shown in Fig. 9. However, no signal was detected in the dark. It can be seen that the surface oxygen molecules will be electronically reduced to O₂^{•-} only when the sample is exposed to ultraviolet irradiation. Furthermore, a peak with an intensity ratio of 1:2:2:1 is obviously shown in Fig. 10(b), indicating the formation of ·OH on the catalyst surface under ultraviolet irradiation. According to the above analysis, it can be reasonably concluded that the formed O₂^{•-} and ·OH are the primary active species participating in the oxidation of Hg⁰.

Fig. 10 depicts a possible mechanism of Hg⁰ removal catalyzed by sulfur defect-enriched W-MoS₂ in which the transfer of photogenerated

electron-hole pairs can be clearly seen. As indicated by the above experiments, the sulfur defect-enriched W-MoS₂-9 h sample showed efficient photocatalytic removal of Hg⁰ performance under both ultraviolet and visible light irradiation. On the one hand, sulfur defects induced by W doping are beneficial to reduce the recombination rate of photo-generated electron-holes, activate molecular oxygen and produce more active species (O₂^{•-} and ·OH). The formed active species of O₂^{•-} and ·OH can oxidize Hg⁰ into HgO effectively under light illumination. On the other hand, the heterojunction formed by W doping can also significantly enhance the photocatalytic performance of the samples. Meanwhile, the specific surface area of doped samples increased to promote the adsorption of Hg⁰ and thus, achieve its efficient photocatalytic removal capability. All of these characteristics endow the W-MoS₂-9 h sample with superior photocatalytic performance. The main reaction equations are as follows:

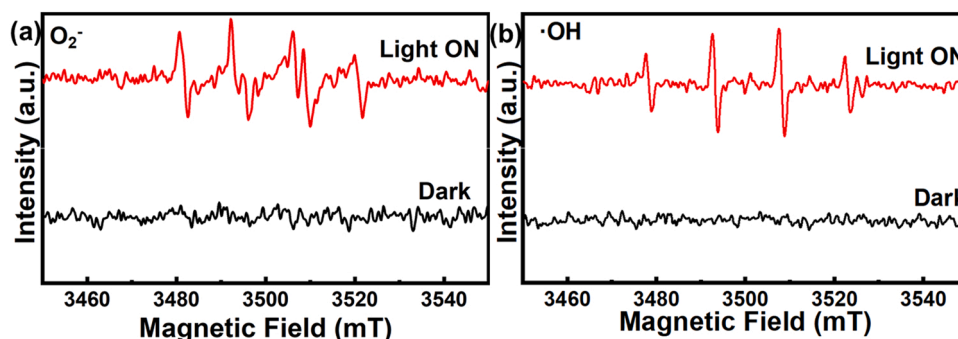


Fig. 9. ESR spectra of O₂^{•-} (a) and ·OH (b) using the W-MoS₂-9 h sample.

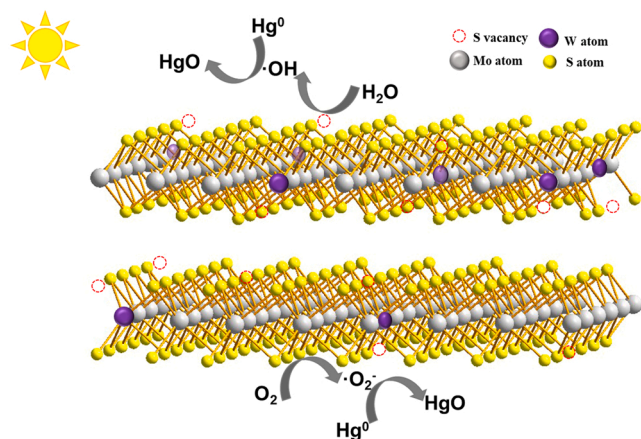
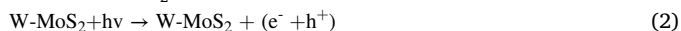


Fig. 10. Proposed mechanism for the photocatalytic oxidation of Hg^0 on the surface of W-MoS_2 .



4. Conclusions

Sulfur defect-enriched W-MoS_2 sample was obtained via tungsten doping from a simple one-step hydrothermal route. Tungsten doping not only promotes the formation of sulfur defects, but also enhances the separation and transfer efficiency of electron-hole pairs, so that the samples can maintain high catalytic activity for a long time. It is also found that the sulfur defects could promote the activation of molecular oxygen and the formation of more active species (O_2^- and $\cdot\text{OH}$), both of which could improve the photocatalytic activity. Besides, the cyclability tests showed that the doped samples have high stability. Compared with pure MoS_2 , the doped sample of W-MoS_2 -9 h exhibited excellent Hg^0 removal efficiencies of 99.03% and 76% under ultraviolet and visible light irradiation, respectively. Thus, this study provides a new direction for the design of efficient transition metal dichalcogenide based photocatalysts, which have good application potential in photocatalytic removal of heavy metals from industrial waste gases.

CRediT authorship contribution statement

Jun Cai: Methodology, Investigation, Writing – original draft, Conceptualization. **Yi Xia:** Supervision, Funding acquisition. **Ruiqi Gang:** Software, Formal analysis. **Sufang He:** Software. **Sridhar Komarneni:** Supervision, Resources.

Declaration of Competing Interest

The authors declare that they have no known competing financial interests or personal relationships that could have appeared to influence the work reported in this paper.

Acknowledgments

This work acknowledges the support from the National Natural Science Foundation of China (62101225). Special project for

international scientific and technological cooperation “Zhihui Yunnan” plan (202103AM140040). Natural Science Foundation of Yunnan Province (202101AU070031, 202101AT070216).

Appendix A. Supporting information

Supplementary data associated with this article can be found in the online version at [doi:10.1016/j.apcatb.2022.121486](https://doi.org/10.1016/j.apcatb.2022.121486).

References

- [1] H. Yang, Z. Xu, M. Fan, A.E. Bland, R.R. Judkins, Adsorbents for capturing mercury in coal-fired boiler flue gas, *J. Hazard Mater.* 146 (2007) 1–11, <https://doi.org/10.1016/j.jhazmat.2007.04.113>.
- [2] R. Hao, C. Li, Z. Wang, Y. Gong, B. Yuan, Y. Zhao, L. Wang, J. Crittenden, Removal of gaseous elemental mercury using thermally catalytic chlorite-persulfate complex, 123508, *Chem. Eng. J.* 391 (2020), 123508, <https://doi.org/10.1016/j.cej.2019.123508>.
- [3] Y. Guan, Y. Liu, Q. Lv, J. Wu, Bismuth-based photocatalyst for photocatalytic oxidation of flue gas mercury removal: a review, *J. Hazard Mater.* 418 (2021), 126280, <https://doi.org/10.1016/j.jhazmat.2021.126280>.
- [4] Q. Hong, Y. Liao, H. Xu, W. Huang, Z. Qu, N. Yan, Stepwise ions incorporation method for continuously activating PbS to recover mercury from Hg^0 -rich flue gas, *Environ. Sci. Technol.* 54 (2020) 11594–11601, <https://doi.org/10.1021/acs.est.0c03335>.
- [5] Q. Huang, X. He, W. Huang, J.R. Reinfelder, Mass-independent fractionation of mercury isotopes during photoreduction of soot particle bound $\text{Hg}(\text{II})$, *Environ. Sci. Technol.* 55 (2021) 13783–13791, <https://doi.org/10.1021/acs.est.1c02679>.
- [6] H. Swaminathan, K. Balasubramanian, Design of “turn-ON and turn-OFF” fluorescence switching based photonic logic gates through multiple input-output models by MoS_2 quantum dots, *J. Colloid Interface Sci.* 540 (2019) 258–264, <https://doi.org/10.1016/j.jcis.2019.01.004>.
- [7] A. Splendiani, L. Sun, Y. Zhang, T. Li, J. Kim, C.Y. Chim, G. Galli, F. Wang, Emerging photoluminescence in monolayer MoS_2 , *Nano Lett.* 10 (2010) 1271–1275, <https://doi.org/10.1021/nl903868w>.
- [8] H. Li, Z. Yin, Q. He, H. Li, X. Huang, G. Lu, D.W. Fam, A.I. Tok, Q. Zhang, H. Zhang, Fabrication of single- and multilayer MoS_2 film-based field-effect transistors for sensing NO at room temperature, *Small* 8 (2012) 63–67, <https://doi.org/10.1002/sml.201101016>.
- [9] B. Radisavljevic, A. Radenovic, J. Brivio, V. Giacometti, A. Kis, Single-layer MoS_2 transistors, *Nat. Nanotechnol.* 6 (2011) 147–150, <https://doi.org/10.1038/nnano.2010.279>.
- [10] M. Velický, P.S. Toth, From two-dimensional materials to their heterostructures: an electrochemist’s perspective, *Appl. Mater. Today* 8 (2017) 68–103, <https://doi.org/10.1016/j.apmt.2017.05.003>.
- [11] M. Chhowalla, H.S. Shin, G. Eda, L.J. Li, K.P. Loh, H. Zhang, The chemistry of two-dimensional layered transition metal dichalcogenide nanosheets, *Nat. Chem.* 5 (2013) 263–275, <https://doi.org/10.1038/nchem.1589>.
- [12] F. Withers, O. Del Pozo-Zamudio, A. Mishchenko, A.P. Rooney, A. Gholinia, K. Watanabe, T. Taniguchi, S.J. Haigh, A.K. Geim, A.I. Tartakovskii, K. S. Novoselov, Light-emitting diodes by band-structure engineering in van der Waals heterostructures, *Nat. Mater.* 14 (2015) 301–306, <https://doi.org/10.1038/nmat4205>.
- [13] Z. Luo, Y. Ouyang, H. Zhang, M. Xiao, J. Ge, Z. Jiang, J. Wang, D. Tang, X. Cao, C. Liu, W. Xing, Chemically activating MoS_2 via spontaneous atomic palladium interfacial doping towards efficient hydrogen evolution, *Nat. Commun.* 9 (2018) 2120, <https://doi.org/10.1038/s41467-018-04501-4>.
- [14] C. Wang, H. Lu, K. Tang, Z. Mao, Q. Li, X. Wang, C. Yan, Atom removal on the basal plane of layered MoS_2 leading to extraordinarily enhanced electrocatalytic performance, *Electrochim. Acta* 336 (2020), 135740, <https://doi.org/10.1016/j.electacta.2020.135740>.
- [15] M. Šarić, J. Rossmeisl, P.G. Moses, Modeling the adsorption of sulfur containing molecules and their hydrodesulfurization intermediates on the Co-promoted MoS_2 catalyst by DFT, *J. Catal.* 358 (2018) 131–140, <https://doi.org/10.1016/j.jcat.2017.12.001>.
- [16] X. Liu, X. Han, Z. Liang, Y. Xue, Y. Zhou, X. Zhang, H. Cui, J. Tian, Phosphorus-doped 1T- MoS_2 decorated nitrogen-doped g-C₃N₄ nanosheets for enhanced photocatalytic nitrogen fixation, *J. Colloid Interface Sci.* 605 (2022) 320–329, <https://doi.org/10.1016/j.jcis.2021.07.111>.
- [17] G. Zhao, W. Ma, X. Wang, Y. Xing, S. Hao, X. Xu, Self-water-absorption-type two-dimensional composite photocatalyst with high-efficiency water absorption and overall water-splitting performance, *Adv. Powder Mater.* 1 (2022), 100008, <https://doi.org/10.1016/j.apmat.2021.09.008>.
- [18] X. Chen, S. Zhang, X. Qian, Z. Liang, Y. Xue, X. Zhang, J. Tian, Y. Han, M. Shao, Enabling efficient electrocatalytic conversion of N_2 to NH_3 by Ti_3C_2 MXene loaded with semi-metallic 1T'- MoS_2 nanosheets, *Appl. Catal. B: Environ.* 310 (2022), 121277, <https://doi.org/10.1016/j.apcatb.2022.121277>.
- [19] J. Ge, D. Zhang, Y. Qin, T. Dou, M. Jiang, F. Zhang, X. Lei, Dual-metallic single Ru and Ni atoms decoration of MoS_2 for high-efficiency hydrogen production, *Appl. Catal. B: Environ.* 298 (2021), 120577, <https://doi.org/10.1016/j.apcatb.2021.120577>.
- [20] X. Hu, J. Jin, Y. Wang, C. Lin, S. Wan, K. Zhang, L. Wang, J.H. Park, Au/ MoS_2 tips as auxiliary rate aligners for the photocatalytic generation of syngas with a tunable

- composition, *Appl. Catal. B: Environ.* 308 (2022), 121219, <https://doi.org/10.1016/j.apcatb.2022.121219>.
- [21] S. Sun, Q. An, M. Watanabe, J. Cheng, H. Ho Kim, T. Akbay, A. Takagaki, T. Ishihara, Highly correlation of CO₂ reduction selectivity and surface electron Accumulation: A case study of Au-MoS₂ and Ag-MoS₂ catalyst, *Appl. Catal. B: Environ.* 271 (2020), 118931, <https://doi.org/10.1016/j.apcatb.2020.118931>.
- [22] F. Withers, T.H. Bointon, D.C. Hudson, M.F. Craciun, S. Russo, Electron transport of WS₂ transistors in a hexagonal boron nitride dielectric environment, *Sci. Rep.* 4 (2014) 4967, <https://doi.org/10.1038/srep04967>.
- [23] X. Wang, Y.-n Zhou, R. Li, L. Wang, L. Tao, P. Ning, Removal of Hg⁰ from a simulated flue gas by photocatalytic oxidation on Fe and Ce co-doped TiO₂ under low temperature, *Chem. Eng. J.* 360 (2019) 1530–1541, <https://doi.org/10.1016/j.cej.2018.10.237>.
- [24] I.S. Jeon, S.J. Kim, W. Song, S. Myung, J. Lim, S.S. Lee, H.-K. Jung, J. Hwang, K.-S. An, One-step synthesis of Zn-doped MoS₂ nanosheets with tunable doping concentration using dopants-loaded seeding promoters for visible-light flexible photodetectors, *J. Alloy. Compd.* 835 (2020), 155383, <https://doi.org/10.1016/j.jallcom.2020.155383>.
- [25] H.-R. Jeong, Y.-K. Lee, Comparison of unsupported WS₂ and MoS₂ catalysts for slurry phase hydrocracking of vacuum residue, *Appl. Catal. A: Gen.* 572 (2019) 90–96, <https://doi.org/10.1016/j.apcata.2018.12.019>.
- [26] W. Wu, C. Niu, C. Wei, Y. Jia, C. Li, Q. Xu, Activation of MoS₂ basal planes for hydrogen evolution by zinc, *Angew. Chem. Int. Ed. Engl.* 58 (2019) 2029–2033, <https://doi.org/10.1002/ange.201812475>.
- [27] Y. Xia, C. Hu, S. Guo, L. Zhang, M. Wang, J. Peng, L. Xu, J. Wang, Sulfur-vacancy-enriched MoS₂ nanosheets based heterostructures for near-infrared optoelectronic NO₂ sensing, *ACS Appl. Nano Mater.* 3 (2019) 665–673, <https://doi.org/10.1021/acsnano.9b02180>.
- [28] D.A. Reddy, H. Park, R. Ma, D.P. Kumar, M. Lim, T.K. Kim, Heterostructured WS₂-MoS₂ ultrathin nanosheets integrated on CdS nanorods to promote charge separation and migration and improve solar-driven photocatalytic hydrogen evolution, *ChemSusChem* 10 (2017) 1563–1570, <https://doi.org/10.1002/cssc.201601799>.
- [29] B. Ma, P.Y. Guan, Q.Y. Li, M. Zhang, S.Q. Zang, MOF-derived flower-like MoS₂@TiO₂ nanohybrids with enhanced activity for hydrogen evolution, *ACS Appl. Mater. Interfaces* 8 (2016) 26794–26800, <https://doi.org/10.1021/acsami.6b08740>.
- [30] W. Yu, Xa Chen, W. Mei, C. Chen, Y. Tsang, Photocatalytic and electrochemical performance of three-Dimensional reduced graphene Oxide/WS₂/Mg-doped ZnO composites, *Appl. Surf. Sci.* 400 (2017) 129–138, <https://doi.org/10.1016/j.apsusc.2016.12.138>.
- [31] J. Shi, R. Tong, X. Zhou, Y. Gong, Z. Zhang, Q. Ji, Y. Zhang, Q. Fang, L. Gu, X. Wang, Z. Liu, Y. Zhang, Temperature-mediated selective growth of MoS₂/WS₂ and WS₂/MoS₂ vertical stacks on Au foils for direct photocatalytic applications, *Adv. Mater.* 28 (2016) 10664–10672, <https://doi.org/10.1002/adma.201603174>.
- [32] Y. Sang, Z. Zhao, M. Zhao, P. Hao, Y. Leng, H. Liu, From UV to near-infrared, WS₂ nanosheet: a novel photocatalyst for full solar light spectrum photodegradation, *Adv. Mater.* 27 (2015) 363–369, <https://doi.org/10.1002/adma.201403264>.
- [33] Y. Ma, J. Li, E. Liu, J. Wan, X. Hu, J. Fan, High efficiency for H₂ evolution and NO removal over the Ag nanoparticles bridged g-C₃N₄ and WS₂ heterojunction photocatalysts, *Appl. Catal. B: Environ.* 219 (2017) 467–478, <https://doi.org/10.1016/j.apcatb.2017.07.061>.
- [34] M.S. Akple, J. Low, S. Wageh, A.A. Al-Ghamdi, J. Yu, J. Zhang, Enhanced visible light photocatalytic H₂-production of g-C₃N₄/WS₂ composite heterostructures, *Appl. Surf. Sci.* 358 (2015) 196–203, <https://doi.org/10.1016/j.apsusc.2015.08.250>.
- [35] H.S. Matte, A. Gomathi, A.K. Manna, D.J. Late, R. Datta, S.K. Pati, C.N. Rao, MoS₂ and WS₂ analogues of graphene, *Angew. Chem. Int. Ed. Engl.*, 49 (2010) 4059–4062, <https://doi.org/10.1002/anie.201000009>.
- [36] J. Wang, H. Deng, X. Li, C. Yang, Y. Xia, Visible-light photocatalysis enhanced room-temperature formaldehyde gas sensing by MoS₂/rGO hybrids, *Sens. Actuators B: Chem.* 304 (2020), 127137, <https://doi.org/10.1016/j.snb.2019.127317>.
- [37] Y. Zou, J.W. Shi, D. Ma, Z. Fan, L. Cheng, D. Sun, Z. Wang, C. Niu, WS₂/Graphitic carbon nitride heterojunction nanosheets decorated with CdS quantum dots for photocatalytic hydrogen production, *ChemSusChem* 11 (2018) 1187–1197, <https://doi.org/10.1002/cssc.201800053>.
- [38] W. Wu, C. Niu, P. Yan, F. Shi, C. Ma, X. Yang, Y. Jia, J. Chen, M.I. Ahmed, C. Zhao, Q. Xu, Building of sub-monolayer MoS_{2-x} structure to circumvent the scaling relations in N₂-to-NH₃ electrocatalysis, *Appl. Catal. B: Environ.* 298 (2021), 120615, <https://doi.org/10.1016/j.apcatb.2021.120615>.
- [39] F. Wang, J. Wang, S. Guo, J. Zhang, Z. Hu, J. Chu, Tuning coupling behavior of stacked heterostructures based on MoS₂, WS₂, and WSe₂, *Sci. Rep.* 7 (2017) 44712, <https://doi.org/10.1038/srep44712>.
- [40] B. Mahler, V. Hoepfner, K. Liao, G.A. Ozin, Colloidal synthesis of 1T-WS₂ and 2H-WS₂ nanosheets: applications for photocatalytic hydrogen evolution, *J. Am. Chem. Soc.* 136 (2014) 14121–14127, <https://doi.org/10.1021/ja506261t>.
- [41] Y. Zhong, Y. Shao, F. Ma, Y. Wu, B. Huang, X. Hao, Band-gap-matched CdSe QD/WS₂ nanosheet composite: size-controlled photocatalyst for high-efficiency water splitting, *Nano Energy* 31 (2017) 84–89, <https://doi.org/10.1016/j.nanoen.2016.11.011>.
- [42] L. Zhang, J. Liang, Y. Wang, T. Mou, Y. Lin, L. Yue, T. Li, Q. Liu, Y. Luo, N. Li, B. Tang, Y. Liu, S. Gao, A.A. Alshehri, X. Guo, D. Ma, X. Sun, High-performance electrochemical NO reduction into NH₃ by MoS₂ nanosheet, *Angew. Chem. Int. Ed. Engl.* (2021) 80599, <https://doi.org/10.1002/ange.202110879>.
- [43] L. Fan, S. Lei, H.M. Kheimeh Sari, L. Zhong, A. Kakimov, J. Wang, J. Chen, D. Liu, L. Huang, J. Hu, L. Lin, X. Li, Controllable S-Vacancies of monolayered Mo-S nanocrystals for highly harvesting lithium storage, *Nano Energy* 78 (2020), 105235, <https://doi.org/10.1016/j.nanoen.2020.105235>.
- [44] Y. Guan, J. Wu, Y. Lin, Q. Liu, Y. Qi, W. Pan, P. He, X. Qi, R. Wang, Z. Ji, Solvent-exfoliation of transition-metal dichalcogenide MoS₂ to provide more active sites for enhancing photocatalytic performance of BiOI₃/g-C₃N₄ photocatalyst, *Appl. Surf. Sci.* 481 (2019) 838–851, <https://doi.org/10.1016/j.apsusc.2019.03.177>.
- [45] Y.-n Zhou, R. Li, L. Tao, R. Li, X. Wang, P. Ning, Solvents mediated-synthesis of 3D-BiOX (X = Cl, Br, I) microspheres for photocatalytic removal of gaseous Hg⁰ from the zinc smelting flue gas, *Fuel* 268 (2020), 117211, <https://doi.org/10.1016/j.fuel.2020.117211>.
- [46] Y. Zhang, P. Ning, X. Wang, L. Wang, Y. Ma, Q. Ma, Y. Xie, High efficiency of Mn–Ce-modified TiO₂ catalysts for the low-temperature oxidation of Hg⁰ under a reducing atmosphere, *Appl. Organomet. Chem.* 33 (2019) 4866, <https://doi.org/10.1002/aoc.4866>.
- [47] T. Jia, J. Wu, Y. Xiao, Q. Liu, Q. Wu, Y. Qi, X. Qi, Self-grown oxygen vacancies-rich CeO₂/BiOBr Z-scheme heterojunction decorated with rGO as charge transfer channel for enhanced photocatalytic oxidation of elemental mercury, *J. Colloid Interface Sci.* 587 (2021) 402–416, <https://doi.org/10.1016/j.jcis.2020.12.005>.
- [48] Y. Ling, X. Man, W. Zhang, D. Wang, J. Wu, Q. Liu, M. Gu, Y. Lin, P. He, T. Jia, Molybdenum trioxide impregnated carbon aerogel for gaseous elemental mercury removal, *Korean J. Chem. Eng.* 37 (2020) 641–651, <https://doi.org/10.1007/s11814-020-0481-x>.
- [49] P. He, X. Zhao, F. Luo, Y. Zhang, J. Wei, T. Xu, J. Wu, N. Chen, Magnetically recyclable Fe₃O₄ doped flower-like MoS₂: Efficient removal of elemental mercury, *Fuel* 282 (2020), 118728, <https://doi.org/10.1016/j.fuel.2020.118728>.
- [50] H. Cheng, J. Wu, F. Tian, L. Zhao, Z. Ji, F. Li, Q. Li, Z. Guan, T. Zhou, In-situ crystallization for fabrication of BiOI/Bi₄O₅I₂ heterojunction for enhanced visible-light photocatalytic performance, *Mater. Lett.* 232 (2018) 191–195, <https://doi.org/10.1016/j.matlet.2018.08.119>.
- [51] J. Wu, K. Xu, Q. Liu, Z. Ji, C. Qu, H. XuemeiQi, Y. Zhang, P. Guan, L. He, Zhu, Controlling dominantly reactive (010) facets and impurity level by in-situ reduction of BiOI₃ for enhancing photocatalytic activity, *Appl. Catal. B: Environ.* 232 (2018) 135–145, <https://doi.org/10.1016/j.apcatb.2018.03.046>.